

Original Article

Intrinsically ^{89}Zr -labeled $\text{Gd}_2\text{O}_2\text{S}:\text{Eu}$ nanophosphors with high *in vivo* stability for dual-modality imaging

Fanrong Ai^{1,2*}, Shreya Goel^{3*}, Yonghua Zhan^{2,4*}, Hector F Valdovinos⁵, Feng Chen², Todd E Barnhart⁵, Weibo Cai^{2,3,5,6}

¹School of Mechanical & Electrical Engineering, Nanchang University, Jiangxi, China; Departments of ²Radiology, ⁵Medical Physics; ³Materials Science Program, University of Wisconsin-Madison, Madison, WI; ⁴Engineering Research Centre of Molecular and Neuro Imaging of the Ministry of Education, School of Life Science and Technology, Xidian University, Xi'an, Shaanxi, China; ⁶University of Wisconsin Carbone Cancer Centre, Madison, WI. *Equal contributors.

Received September 22, 2016; Accepted November 28, 2016; Epub December 15, 2016; Published December 30, 2016

Abstract: Radioluminescence imaging (RLI) employs high energy particles from radioisotope decay for *in situ* excitation of selected nanophosphors. Co-injection of radiopharmaceuticals and nanophosphors suffers from suboptimal RL efficiency owing to the large separation between the source and the emitter. In addition, vastly different pharmacokinetic profiles of the two further impede the practical applications of this approach. To overcome the above challenges, chelator-free radiolabeled nanophosphors with excellent RL efficiency and dual-modality imaging capabilities have been proposed. Abundant O^{2-} donors on $\text{Gd}_2\text{O}_2\text{S}:\text{Eu}$ could intrinsically chelate oxophilic radionuclide ^{89}Zr with ~80 % labeling yield. Positron emission tomography demonstrated superb long-term radiostability of [^{89}Zr] $\text{Gd}_2\text{O}_2\text{S}:\text{Eu}$ @PEG nanoparticles *in vivo*, and a conventional optical imaging system was used to study radioluminescence properties of [^{89}Zr] $\text{Gd}_2\text{O}_2\text{S}:\text{Eu}$ @PEG nanoparticles *in vitro* and *in vivo*.

Keywords: Radioluminescence, gadolinium oxysulfide, positron emission tomography, multimodality imaging, nanophosphors

Introduction

Radioluminescent lanthanide-doped nanophosphors (RLNPs), such as Eu^{3+} doped gadolinium oxysulfides have emerged as promising candidates for biological imaging, owing to their high photochemical stability, tunable fluorescence emission; negligible photobleaching and large Stokes shift [1-3]. Red to near-infrared (NIR)-emitting RLNPs rely on excitation by high energy ionizing radiation, such as those employed in X-ray computed tomography (CT) and positron emission tomography (PET), to visualize biological processes, with enhanced tissue penetration and signal-to-noise ratios [1]. Herein, we report a facile procedure for the synthesis of intrinsically radiolabeled, water-soluble RLNPs, specifically $\text{Gd}_2\text{O}_2\text{S}:\text{Eu}^{3+}$ nanoparticles for internally activatable radioluminescence imaging (RLI). $\text{Gd}_2\text{O}_2\text{S}:\text{Eu}^{3+}$ nanoparticles are well-known scintillators that absorb UV or X-

rays strongly, and re-emit red light with a high quantum yield, useful for optical luminescence and radioluminescence [4, 5]. Additionally, the strong transverse relaxivity of Gd element can be harnessed for T_1 -weighted MRI and thus, $\text{Gd}_2\text{O}_2\text{S}:\text{Eu}^{3+}$ nanophosphors are promising candidates as multimodal imaging agents [6]. Activation of RLNPs ($\text{Ln}_2\text{O}_2\text{S}$; Ln = La-Lu) by radioisotopes such as PET tracers is a rapidly emerging concept [7, 8]. Compared to X-ray excited RL, radioisotope excited RLI offers several advantages, namely, facile operation using the conventional optical imaging systems without additional bulky hardware, and easy multiplexing with PET for co-registration of molecular events [9, 10]. However, all the studies till date have reported remote excitation of RLNPs via co-injection of radiopharmaceuticals, whereby RLI efficiency is compromised due to significant spatial distance between the radioisotopes and RLNPs and their different pharmacokinetic pro-

files. Herein, we propose chelator-free ^{89}Zr labeling of $\text{Gd}_2\text{O}_2\text{S}:\text{Eu}$ with excellent radiostability, as well as enhanced radioluminescence efficiency *in vivo*, when compared to $\text{Gd}_2\text{O}_2\text{S}:\text{Eu}$ nanoparticles simply mixed with ^{89}Zr .

Materials and methods

Materials

Gadolinium (III) chloride hexahydrate ($\text{GdCl}_3 \cdot 6\text{H}_2\text{O}$, >99.99%), Europium (III) chloride hexahydrate ($\text{EuCl}_3 \cdot 6\text{H}_2\text{O}$, >99.99%), Sodium diethyldithiocarbamate trihydrate ($\text{Na}(\text{ddtc}) \cdot 3\text{H}_2\text{O}$, >98%), 1,10-Phenanthroline ($\text{C}_{12}\text{H}_8\text{N}_2$, >99%) were purchased from Sigma-Aldrich. Oleic acid, oleylamine, 1-octadecene, cyclohexane, chloroform, acetone and absolute ethanol were purchased from Fisher Scientific. DSPE-PEG_{5k}-Mal was obtained from Creative PEGWorks. All chemicals were used as received without further purification.

Synthesis of precursor $\text{Gd}(\text{ddtc})_3(\text{Phen})$ and $\text{Eu}(\text{ddtc})_3(\text{Phen})$

The precursors $\text{Gd}(\text{ddtc})_3(\text{Phen})$ and $\text{Eu}(\text{ddtc})_3(\text{Phen})$ were synthesized via a slightly modified method developed by Formanovskii and group [11]. In a typical procedure, solution of $\text{GdCl}_3 \cdot 6\text{H}_2\text{O}$ in water (1 mmol, 10 ml) was added to a solution of 1,10-Phenanthroline in boiling water (1 mmol, 20 mL) under vigorous stirring. Then, an aqueous solution of $\text{Na}(\text{ddtc}) \cdot 3\text{H}_2\text{O}$ (3 mmol dissolved in 20 mL of distilled water followed by filtration) was added dropwise to the above solution under constant stirring. The yellow-colored $\text{Gd}(\text{ddtc})_3(\text{Phen})$ precipitate was collected by centrifugation and dried in vacuum at room temperature for further use. Deep orange-colored $\text{Eu}(\text{ddtc})_3(\text{Phen})$ precipitate was produced by a similar procedure, using $\text{EuCl}_3 \cdot 6\text{H}_2\text{O}$ to substitute $\text{GdCl}_3 \cdot 6\text{H}_2\text{O}$.

Preparation of monodispersed $\text{Gd}_2\text{O}_2\text{S}:\text{Eu}$ nanoparticles

The $\text{Gd}_2\text{O}_2\text{S}:\text{Eu}$ nanoparticles were synthesized via co-thermal decomposition of precursors $\text{Gd}(\text{ddtc})_3(\text{Phen})$ and $\text{Eu}(\text{ddtc})_3(\text{Phen})$ in 1-octadecene in the presence of oleic acid and oleylamine [12, 13]. In a typical procedure, 0.5 mmol $\text{Gd}(\text{ddtc})_3(\text{Phen})$ and 0.05 mmol $\text{Eu}(\text{ddtc})_3(\text{Phen})$ were added to a mixture of 30 mmol of oleylamine, 5 mmol of oleic acid, and

30 mmol of octadecene at room temperature, under constant stirring. The mixture was heated to 120 °C and degassed for ~30 min, resulting in a homogeneous, clear green-yellow solution. Then the solution was rapidly heated to 290 °C, over 5 min and kept for 2 h. After the solution was cooled down to 70 °C, the product $\text{Gd}_2\text{O}_2\text{S}:\text{Eu}$ nanoparticles were precipitated by adding an excess amount of ethanol and collected by centrifugation. The as-synthesized $\text{Gd}_2\text{O}_2\text{S}:\text{Eu}$ nanoparticles were dried in a vacuum oven at room temperature and finally re-dispersed in chloroform for further use.

Preparation of $\text{Gd}_2\text{O}_2\text{S}:\text{Eu}@\text{PEG}$ nanoparticles

20 mg of DSPE-PEG_{5k}-Mal was dissolved 2 mL of chloroform, then added to 1 mL of 5 mg/mL $\text{Gd}_2\text{O}_2\text{S}:\text{Eu}$ chloroform solution with ultrasonication. After stirring for overnight at room temperature, the solvent was evaporated under a stream of nitrogen. The obtained $\text{Gd}_2\text{O}_2\text{S}:\text{Eu}@\text{PEG}$ nanoparticles were re-dispersed in 5 mL H_2O with the aid of ultrasonication for 10 min. The resulting dispersion was filtered through a 0.2 μm membrane filter and kept at 4 °C for further use.

Characterization

The morphology of the nanoparticles was observed by a transmission electron microscope (TEM; FEI Tecnai T12) operating at 120 kV accelerating voltage. TEM samples were prepared by dropping colloidal dispersion of nanoparticles onto carbon-coated copper grids. The crystalline phases of the nanoparticles were identified using a Bruker D8 focus X-ray powder diffractometer with $\text{Cu K}\alpha$ radiation ($\lambda = 0.15405 \text{ nm}$). Fourier Transform Infrared Spectroscopy (FT-IR) was performed on a Perkin-Elmer 580B infrared spectrophotometer using the KBr pellet technique. Photoluminescence (PL) excitation and emission spectra were obtained using a Thermo-Spectronic AB2 luminescence spectrometer.

^{89}Zr production

^{89}Zr -oxalate was produced as reported previously [14]. Briefly, natural yttrium-89 (^{89}Y) foil (250 μm , 99.9%) was irradiated with a 8-10 μA proton beam, yielding ^{89}Zr via the $^{89}\text{Y}(\text{p,n})^{89}\text{Zr}$ reaction, in a 16 MeV GE PETtrace cyclotron at the University of Wisconsin-Madison. After iso-

tope separation and purification, the specific activity of the obtained ^{89}Zr -oxalate was higher than 20 GBq/ μmol of Zr.

Chelator-free ^{89}Zr labeling of $\text{Gd}_2\text{O}_3\text{:Eu@PEG}$ nanoparticles

For ^{89}Zr labeling, 200 μL of $\text{Gd}_2\text{O}_3\text{:Eu@PEG}$ with various concentrations (1 mg/mL, 0.1 mg/mL or 0.01 mg/mL) in HEPES buffer (0.1 M, pH 7), was mixed with 100 μCi (or 3.7 MBq) of ^{89}Zr -oxalate. The pH of the solution was adjusted to different values (pH 2, 7 or 9) using 2 M Na_2CO_3 and ^{89}Zr labeling was carried out at various temperatures (25°C, 37°C or 75°C). Radiolabeling yield was quantified at different time points (from 15 min to 3 h), using thin layer chromatography (TLC) on silica backed gel plates.

In vitro serum stability study of [^{89}Zr] $\text{Gd}_2\text{O}_3\text{:Eu@PEG}$

To study the stability of ^{89}Zr bound to $\text{Gd}_2\text{O}_3\text{:Eu@PEG}$ nanoparticles *in vitro*, 50 μL of [^{89}Zr] $\text{Gd}_2\text{O}_3\text{:Eu@PEG}$ was incubated in 2X whole mouse serum (50 μL) at 37 °C under constant shaking (550 rpm) for 48 h. Aliquots of 15 μL were taken at each time point, and purified by using a 100 kDa filter. The radioactivity of the filtrate and that retained in the filter was measured by using a gamma counter.

In vivo radiostability study of [^{89}Zr] $\text{Gd}_2\text{O}_3\text{:Eu@PEG}$ by PET imaging

To assess the *in vivo* radiostability of [^{89}Zr] $\text{Gd}_2\text{O}_3\text{:Eu@PEG}$, 100 μCi (or 3.7 MBq) of [^{89}Zr] $\text{Gd}_2\text{O}_3\text{:Eu@PEG}$ or free ^{89}Zr in PBS (to serve as control) was injected intravenously into separate cohorts of healthy Balb/c mice ($n = 3$). PET imaging was carried out at various time-points on a microPET/microCT Inveon rodent model scanner (Siemens Medical Solutions USA, Inc.). Maximum intensity projection (MIP) and region-of-interest (ROI) analysis was performed using vendor software (Inveon Research Workplace), after decay-correction.

Ex vivo biodistribution studies

After the last *in vivo* PET scans on day 7 p.i., mice in both the groups were sacrificed and the following organs were explanted; blood, skin, muscle, bone, heart, lung, liver, kidneys, spleen, pancreas, stomach, intestines, tail, brain. Ea-

ch sample was collected and wet-weighted. The radioactivity accumulated in each organ was measured using a gamma counter, and expressed as percent injected dose per gram (%ID/g).

In vivo radioluminescence imaging with [^{89}Zr] $\text{Gd}_2\text{O}_3\text{:Eu@PEG}$

For *in vivo* radioluminescence imaging, 40 μL (~50 μCi or 1.85 MBq) of [^{89}Zr] $\text{Gd}_2\text{O}_3\text{:Eu@PEG}$ in PBS was injected subcutaneously into nude mice. For the control groups, 40 μL of $\text{Gd}_2\text{O}_3\text{:Eu@PEG}$ in PBS mixed with 50 μCi ^{89}Zr , and 50 μCi ^{89}Zr in 40 μL PBS, were injected subcutaneously in different regions of the mouse. *In vivo* luminescence imaging was performed using the Xenogen IVIS Spectrum imaging system (Caliper Life Sciences) at different time points, (Ex: closed, Em: Open or 620 nm).

Results and discussion

Synthesis and characterization of $\text{Gd}_2\text{O}_3\text{:Eu}$ and $\text{Gd}_2\text{O}_3\text{:Eu@PEG}$

Conventional routes for synthesis of lanthanide oxysulfide nanoparticles require treatment with sulphur [5, 15] or H_2S gas [6] at elevated temperatures (over 900 °C) and are limited in their ability to produce stable, monodispersed nanocrystals for biological applications. In this study, $\text{Gd}_2\text{O}_3\text{:Eu}$ nanoparticles were synthesized via co-thermal decomposition of precursors, $\text{Gd}(\text{ddtc})_3(\text{Phen})$ and $\text{Eu}(\text{ddtc})_3(\text{Phen})$ in 1-octadecene in the presence of oleic acid and oleylamine. TEM images confirmed the size of $\text{Gd}_2\text{O}_3\text{:Eu}$ nanoparticles to be ~13 nm (**Figure 1A**), in good agreement with the slightly larger hydrodynamic diameter of ~17 nm (pink curve; **Figure 1C**). X-ray diffraction (XRD) spectrum (**Figure 1D**) of the nanoparticles corresponded to those of the standard hexagonal phase of $\text{Gd}_2\text{O}_3\text{S}$ (JCPDS 26-1422) with a slight shift towards higher 2θ values resulting from the doping of Eu^{3+} ions. Gd and Eu atoms readily form symmetrical solid solutions owing to similar crystal structures and atomic radii. Doping of Eu^{3+} atoms with a slightly smaller radius results in a decrease in the lattice constant and thus, a concomitant shift in the characteristic peaks of $\text{Gd}_2\text{O}_3\text{S:Eu}$ to higher 2θ values compared to $\text{Gd}_2\text{O}_3\text{S}$. As-synthesized $\text{Gd}_2\text{O}_3\text{:Eu}$ nanoparticles, coated with oleic acid/oleylamine could be well dispersed in nonpolar organic solvents. To improve their biological

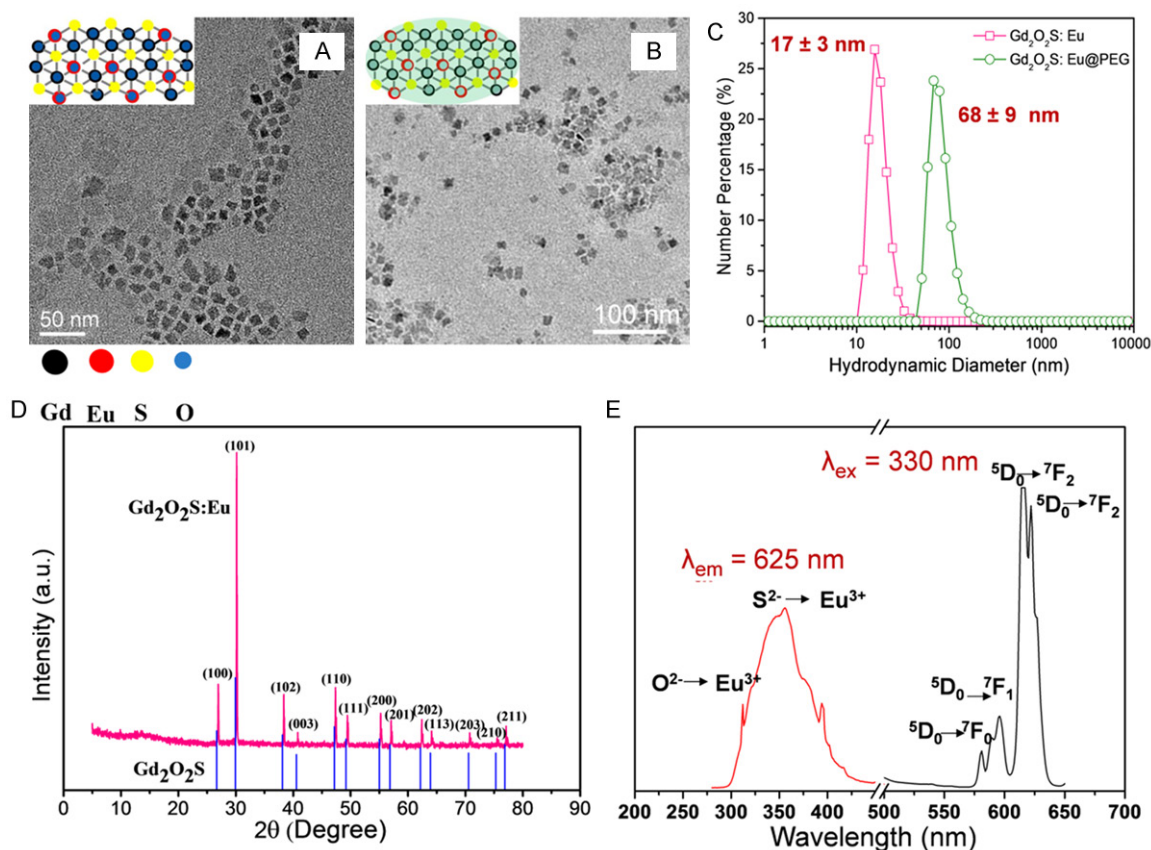


Figure 1. TEM images of (A) as-synthesized $\text{Gd}_2\text{O}_2\text{S}:\text{Eu}^{3+}$ dispersed in chloroform (scale bar: 50 nm), and (B) surface-modified $\text{Gd}_2\text{O}_2\text{S}:\text{Eu}^{3+}$ nanoparticles dispersed in water (scale bar: 100 nm). Insets show schematic of as-synthesized $\text{Gd}_2\text{O}_2\text{S}:\text{Eu}^{3+}$ and $\text{Gd}_2\text{O}_2\text{S}:\text{Eu}^{3+}$ nanoparticles. (C) DLS measurements indicating the hydrodynamic size distributions of $\text{Gd}_2\text{O}_2\text{S}:\text{Eu}^{3+}$ nanoparticles before (pink) and after PEGylation (green). (D) XRD spectrum, and (E) excitation (red) and emission (black) spectra of $\text{Gd}_2\text{O}_2\text{S}:\text{Eu}^{3+}$ nanoparticles.

applications, the nanoparticles were transferred to aqueous media using the well-established phospholipid surface modification strategy [16]. Nanoparticles initially dispersed in chloroform were modified with amphiphilic DS-PE-PEG_{5k}-Mal via hydrophobic van der Waals interactions. PEGylated $\text{Gd}_2\text{O}_2\text{S}:\text{Eu}$ nanoparticles ($\text{Gd}_2\text{O}_2\text{S}:\text{Eu}@\text{PEG}$) maintained their morphology (Figure 1B) and could be stably dispersed in aqueous solutions, displaying an increased hydrodynamic radius of ~ 68 nm (green curve, Figure 1C), with a narrow size distribution.

Figure 1E shows the excitation and emission spectra of $\text{Gd}_2\text{O}_2\text{S}:\text{Eu}^{3+}$ nanoparticles. The excitation spectrum (Figure 1E, red), is composed of a broad excitation band ranging from 300 to 400 nm, corresponding to the charge transfer band (CTB) [5], and narrow lines between 400

to 500 nm. A weak peak at 310 nm and a stronger one around 350 nm, can be attributed to the charge transitions from $\text{O}^{2-} \rightarrow \text{Eu}^{3+}$ and $\text{S}^{2-} \rightarrow \text{Eu}^{3+}$, respectively. The narrow lines observed between 400 and 500 nm correspond to the transitions between 4f levels of Eu^{3+} [6]. Upon excitation at 330 nm, the recorded emission spectrum (Figure 1E, black) exhibited characteristic Eu^{3+} $^5\text{D}_0 \rightarrow ^7\text{F}_j$ ($j = 0-4$) transitions. The strongest red emissions at 615 and 625 nm result from the $^5\text{D}_0 \rightarrow ^7\text{F}_2$ magnetic-dipole and electric dipole transition of Eu^{3+} . The emissions at 581 nm were attributed to $^5\text{D}_0 \rightarrow ^7\text{F}_0$, and those at 589 and 596 nm were attributed $^5\text{D}_0 \rightarrow ^7\text{F}_1$ [3].

Radioluminescence of $\text{Gd}_2\text{O}_2\text{S}:\text{Eu}$ nanophosphors makes them an attractive candidate for multimodality molecular imaging. While X-ray excited radioluminescence of nanophosphors

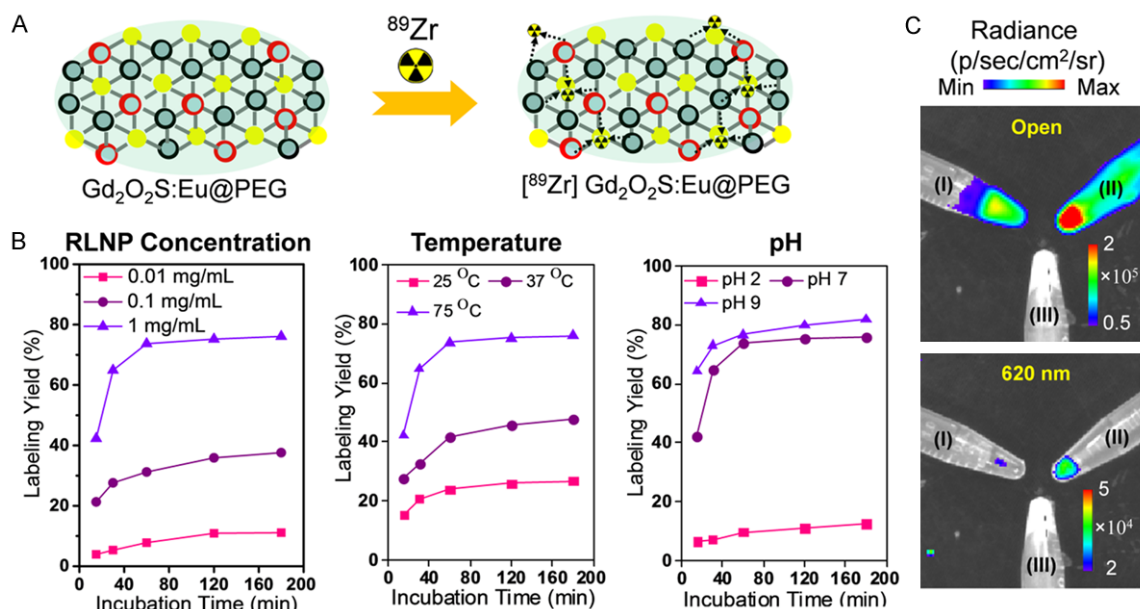


Figure 2. A. Schematic depiction of chelator-free ^{89}Zr -labeling of $\text{Gd}_2\text{O}_2\text{S}:\text{Eu}@\text{PEG}$ nanoparticles. Oxophilic ^{89}Zr is stably chelated by the deprotonated O^{2-} centers on the nanoparticles. B. Influence of nanoparticle concentration, temperature, and pH on radiolabeling yields with time. C. *In vitro* radioluminescence imaging of (I) ^{89}Zr , (II) $[^{89}\text{Zr}] \text{Gd}_2\text{O}_2\text{S}:\text{Eu}@\text{PEG}$ and (III) $\text{Gd}_2\text{O}_2\text{S}:\text{Eu}@\text{PEG}$ nanoparticles, using open and 620 nm emission filters.

is well established, gamma rays derived from the radioactive decay of clinically relevant isotopes can also be used as excitation source. A well-known PET isotope, zirconium-89 (^{89}Zr , $t_{1/2} = 78.4 \text{ h}$; β^+ branching ratio: 23 %) was employed to evaluate the dependence of radioluminescence of $\text{Gd}_2\text{O}_2\text{S}:\text{Eu}$ nanophosphors on various parameters, such as nanoparticle concentration, radioactivity, and the distance between the isotope and nanoparticles. Eppendorf tubes containing the nanoparticles and isotope were placed next to each other and imaged using a conventional small animal optical imaging system (IVIS Spectrum, PerkinElmer, USA; Excitation filter: closed; Emission filter: 620 nm). To prevent interference from the Cerenkov luminescence (CL) from ^{89}Zr , a black tube was employed. Excitation of $\text{Gd}_2\text{O}_2\text{S}:\text{Eu}$ nanoparticles by ^{89}Zr was successfully observed, whereby increasing the nanoparticle concentration or radioactivity increased the intensity of the emission signals (Figures S1 and S2, ESI). Although, remote excitation of quantum dots [17] and nanophosphors [1, 9, 10], via co-injected radioisotopes has been reported previously for RL induction, distance between the donor and the receptor significantly influences the RL intensity. While enhanced emission was observed when the radiation source and RLNP

were in close proximity (Figure S3A, ESI), increasing the spatial distance drastically reduced the radioluminescence intensity. At a separation of $\sim 15 \text{ mm}$, almost no signal could be observed from the RLNP (Figure S3D, ESI).

Chelator-free ^{89}Zr -labeling of $\text{Gd}_2\text{O}_2\text{S}:\text{Eu}$ nanoparticles

In an effort to improve the RL efficiency by minimizing the interaction distance, $\text{Gd}_2\text{O}_2\text{S}:\text{Eu}$ nanoparticles were intrinsically radiolabeled with ^{89}Zr , by exploiting the oxophilic nature of the radionuclide and the abundant O^{2-} donors on the nanoparticle surface (Figure 2A). $\text{Gd}_2\text{O}_2\text{S}:\text{Eu}@\text{PEG}$ nanoparticles were incubated with ^{89}Zr -oxalate in HEPES buffer (0.1 M) with constant stirring, following our previous work with intrinsically ^{89}Zr -labeled silica nanoparticles [18, 19]. Thin layer chromatography (TLC) was employed to study the influence of different parameters (pH, temperature and nanoparticle concentration) on the radiolabeling yield over time. As expected, ^{89}Zr labeling yield was nanoparticle concentration and temperature dependent, where higher concentration and temperature resulted in higher radiolabeling yields (Figure 2B). In addition, to study the role of deprotonated O^{2-} ions on the radiolabeling

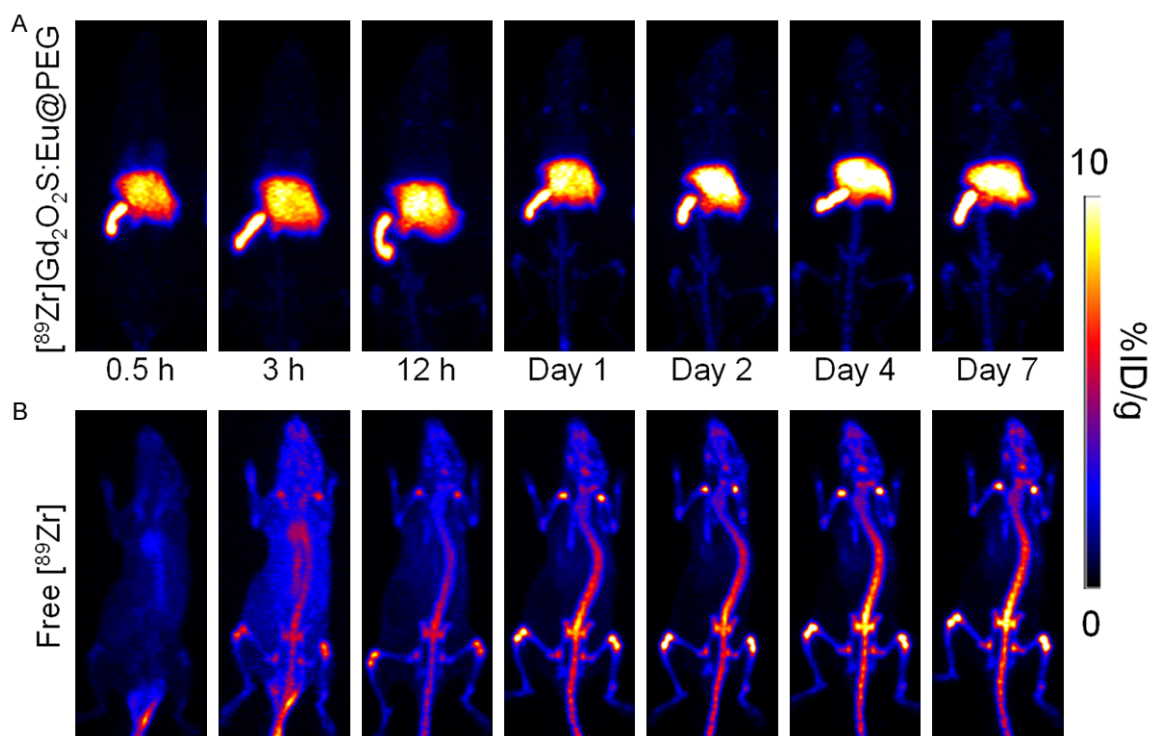


Figure 3. *In vivo* serial coronal MIP PET imaging of Balb/c mice, intravenously injected with 100 μCi of (A) ^{89}Zr $\text{Gd}_2\text{O}_2\text{S}:\text{Eu@PEG}$, and (B) ^{89}Zr -oxalate in PBS. ($n = 3$).

yields, the pH of the solution was tuned to 2-3 to ensure complete protonation of the O^{2-} . As expected, the yield reduced drastically, reaching a maximum of 12 % after 3 h of incubation. In contrast, at pH values 7-8, ~43 % ^{89}Zr labeling yield was achieved within 15 min of incubation, which increased to ~76 % in 3 h (**Figure 2**). Increasing the pH further to 9-10 depicted a marginal increase in the radiolabeling yield to ~81 %. However, owing to concerns about ^{89}Zr -oxalate stability and possible formation of hydroxides in highly alkaline solution, pH 7-8 was chosen for further studies.

Intrinsically radiolabeled ^{89}Zr $\text{Gd}_2\text{O}_2\text{S}:\text{Eu@PEG}$ nanoparticles were then tested for their radioluminescence, along with equal quantities of ^{89}Zr (~50 μCi or 1.85 MBq) and $\text{Gd}_2\text{O}_2\text{S}:\text{Eu@PEG}$ solution (40 μL , 1 mg/mL) only controls. Imaging was carried out using open and 620 nm emission filters. As shown in **Figure 2C**, ^{89}Zr $\text{Gd}_2\text{O}_2\text{S}:\text{Eu@PEG}$ displayed higher luminescence intensity than that of ^{89}Zr control (signal attributed to Cerenkov luminescence, a continuous spectrum with peak emission in the UV region). The enhanced optical signal from ^{89}Zr $\text{Gd}_2\text{O}_2\text{S}:\text{Eu@PEG}$ above CL from ^{89}Zr , was attrib-

uted to both UV excitation of doped Eu^{3+} , as well as gamma ray-induced radioluminescence of $\text{Gd}_2\text{O}_2\text{S}:\text{Eu}$ nanophosphors by ^{89}Zr . Stimulation of the characteristic emission spectrum of RLNPs was further confirmed by applying a 620 nm filter, to minimize the influence of the CL component in the emission signal (**Figure 2C**; lower panel). As expected, the signal intensity from the ^{89}Zr control (I) drastically decreased upon application of the filter, since the CL spectrum contributes mostly to emission wavelengths below 600 nm. On the other hand, ^{89}Zr $\text{Gd}_2\text{O}_2\text{S}:\text{Eu@PEG}$ (II) displayed luminescence intensity over and above the CL signal, which can be attributed to the characteristic Eu^{3+} luminescence that appears at 625 nm. Non-radiolabeled $\text{Gd}_2\text{O}_2\text{S}:\text{Eu@PEG}$ nanoparticle control showed no optical signal in either case. The longer emission wavelength from the radioluminescence of ^{89}Zr $\text{Gd}_2\text{O}_2\text{S}:\text{Eu@PEG}$ nanoparticles maybe more beneficial for biological imaging since it overcomes the tissue penetration limitation of UV region emissions of CL. Further investigation into the photophysical phenomena of RLNPs, and optimization of dopant concentrations to improve the RL efficiency of these nanophosphors are warranted.

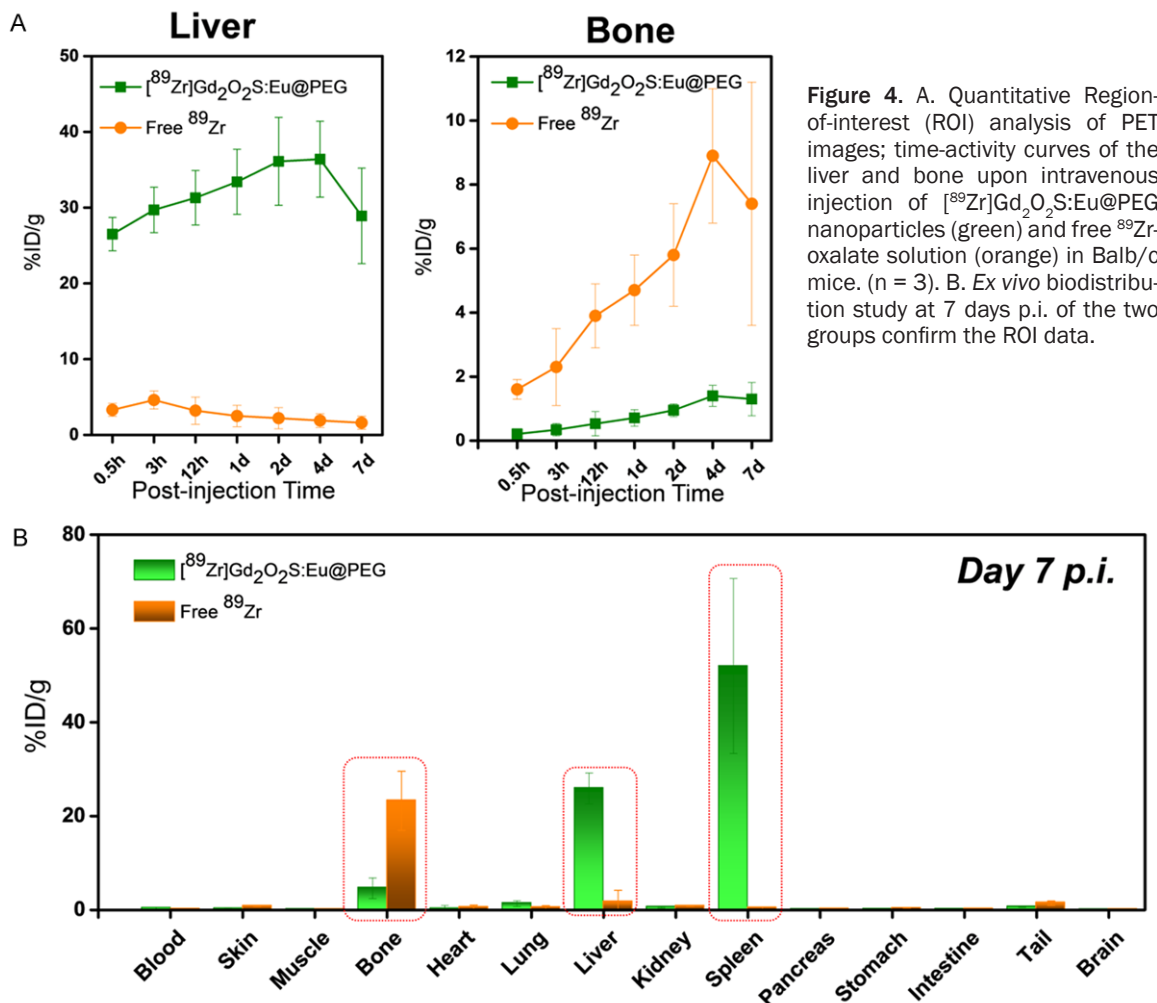


Figure 4. A. Quantitative Region-of-interest (ROI) analysis of PET images; time-activity curves of the liver and bone upon intravenous injection of $^{89}\text{Zr}[\text{Gd}_2\text{O}_2\text{S}:\text{Eu}@\text{PEG}]$ nanoparticles (green) and free ^{89}Zr -oxalate solution (orange) in Balb/c mice. ($n = 3$). B. Ex vivo biodistribution study at 7 days p.i. of the two groups confirm the ROI data.

Radiostability of $^{89}\text{Zr}\text{-Gd}_2\text{O}_2\text{S}:\text{Eu}@\text{PEG}$ nanoparticles

Radiostability of the as-prepared $^{89}\text{Zr}[\text{Gd}_2\text{O}_2\text{S}:\text{Eu}@\text{PEG}]$ nanoparticles was then evaluated *in vitro*. Radiolabeled nanoparticles were incubated in mouse serum at 37°C , over 48 h. No obvious detachment of ^{89}Zr was observed with $\sim 98\%$ of the radioactivity stably bound to the nanoparticles at the end of the test period (Figure S4, ESI). The long half-life of ^{89}Zr (~ 3 days) enables long-term tracking of nanoparticle biodistribution and clearance kinetics *in vivo*. Moreover, ^{89}Zr is a well-known osteophile, with a tendency to accumulate in the bones [20]. Thus, the radiostability of $^{89}\text{Zr}[\text{Gd}_2\text{O}_2\text{S}:\text{Eu}@\text{PEG}]$ can be monitored *in vivo* by dynamic changes in the bone uptake. Accordingly, $100\ \mu\text{Ci}$ (or $3.7\ \text{MBq}$) of $^{89}\text{Zr}[\text{Gd}_2\text{O}_2\text{S}:\text{Eu}@\text{PEG}]$ was intravenously (i.v.) administered in healthy Balb/c mice and *in vivo* biodistribution (and

hence radiostability of the RLNPs) was monitored over a week via serial PET imaging at different time-points post-injection (p.i.). In a separate cohort of mice, free ^{89}Zr -oxalate in PBS was i.v. injected to serve as the control group. As apparent from the maximum intensity projections (Figure 3A), mice injected with $^{89}\text{Zr}[\text{Gd}_2\text{O}_2\text{S}:\text{Eu}@\text{PEG}]$ show excellent radiostability, evidenced by the low bone uptake upto 7 d p.i. Dominant uptake of the nanoparticles was observed in the mononuclear phagocytic (MPS) organs, liver and spleen, characteristic of intravenously injected nanoparticles, larger than the renal clearance threshold of $\sim 6\text{-}7\ \text{nm}$ [21]. On the other hand, mice treated with ^{89}Zr -oxalate control, show distinct signals from the joints and bones.

Region of interest (ROI) quantification of the PET images at different time points p.i. indicated that the bone uptake in mice injected with

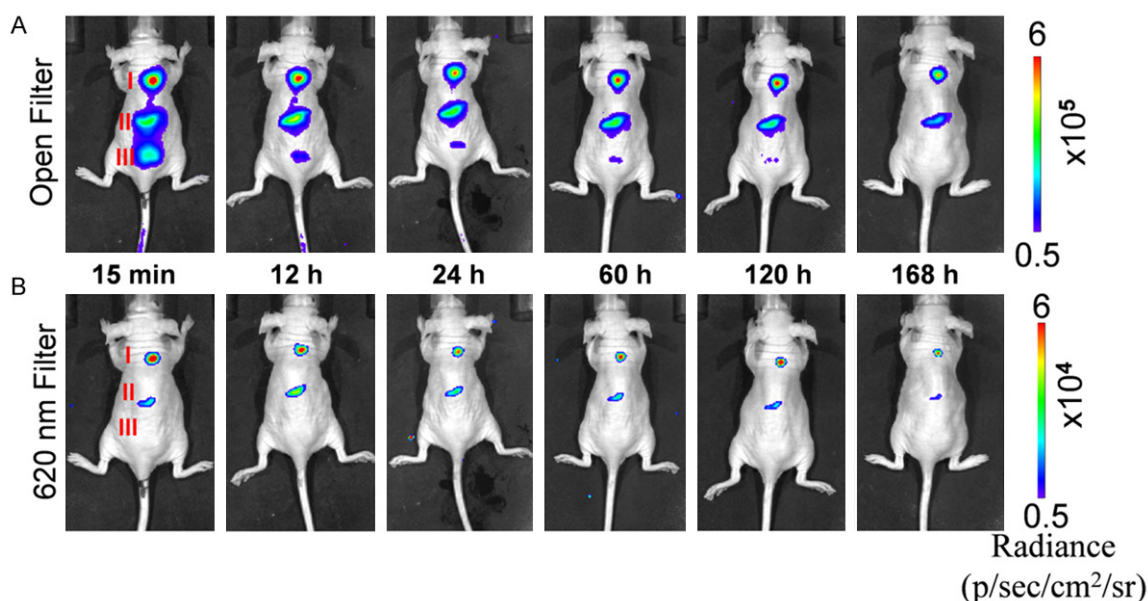


Figure 5. *In vivo* RLI after subcutaneous injection of 50 µCi of (I) $^{89}\text{Zr}[\text{Gd}_2\text{O}_2\text{S}:\text{Eu}@\text{PEG}]$, (II) $\text{Gd}_2\text{O}_2\text{S}:\text{Eu}@\text{PEG} + ^{89}\text{Zr}$, and (III) ^{89}Zr only. Serial luminescence images were obtained at different time-points p.i. with (A) Ex: closed, Em: Open, and (B) Ex: closed, Em: 620 nm filters.

$^{89}\text{Zr}[\text{Gd}_2\text{O}_2\text{S}:\text{Eu}@\text{PEG}]$ was less than 0.5 %ID/g upto 12 h p.i. The bone uptake increases to 1.4 ± 0.3 %ID/g at 4 d p.i., remaining more than 6-fold less than that in mice injected with ^{89}Zr -oxalate (7.4 ± 3.8 %ID/g, 7 day p.i.) (**Figure 4A**). $^{89}\text{Zr}-\text{Gd}_2\text{O}_2\text{S}:\text{Eu}@\text{PEG}$ were rapidly phagocytosed by reticuloendothelial system (RES), as evidenced by a corresponding increase in the liver uptake from 26.5 ± 2.2 %ID/g at 0.5 h p.i. to 36.4 ± 5 %ID/g at day 4 p.i. A slight decrease was observed on day 7 (28.9 ± 6.3 %ID/g) that can be attributed to the hepatic clearance of $^{89}\text{Zr}[\text{Gd}_2\text{O}_2\text{S}:\text{Eu}@\text{PEG}]$. Concomitant decrease in the bone signal (1.3 ± 0.5 %ID/g) ruled out the possibility of ^{89}Zr detachment from the nanophosphors. The results were further corroborated by ex vivo biodistribution studies, day 7 p.i. (**Figure 4B**) Overall, the dynamic changes in ^{89}Zr uptake in the liver and bone confirmed the excellent *in vivo* radiostability of $^{89}\text{Zr}[\text{Gd}_2\text{O}_2\text{S}:\text{Eu}@\text{PEG}]$. Our studies demonstrated that chelator-free ^{89}Zr labeling of metal oxides and oxysulfides can be a useful tool in accurately and quantitatively monitoring the *in vivo* pharmacokinetics and biodistribution of the nanoparticles. In addition, the radiolabeling strategy can be extended to other oxophilic radiometals such as ^{45}Ti , which are difficult to label via traditional chelator-based approaches, and are thus hampered in their clinical applications.

In vivo radioluminescence imaging

The *in vivo* RL efficiency of $^{89}\text{Zr}[\text{Gd}_2\text{O}_2\text{S}:\text{Eu}@\text{PEG}]$ nanoparticles was then studied. 50 µCi of the radiolabeled nanoparticles was subcutaneously injected into nude mice and imaged at various time-points (Excitation filter: blocked; Emission filter: open or 620 nm). Equal amounts of $\text{Gd}_2\text{O}_2\text{S}:\text{Eu}@\text{PEG}$ nanoparticles mixed with ^{89}Zr , as well as ^{89}Zr -oxalate only, were also injected as control. Although the signals from all three samples are high at 15 min p.i., distinct difference can be seen in the intensity between $^{89}\text{Zr}[\text{Gd}_2\text{O}_2\text{S}:\text{Eu}@\text{PEG}]$ (spot I) and control groups (spots II and III). The luminescence signals in all three groups decreased with time, presumably due to radioactive decay of ^{89}Zr . However, the reduction was more significant and rapid in the control groups, when compared to that of $^{89}\text{Zr}[\text{Gd}_2\text{O}_2\text{S}:\text{Eu}@\text{PEG}]$ (**Figure 5A**). This behavior can be attributed to the gradual diffusion of free ^{89}Zr into the surrounding tissue, further testifying that radiolabeled and not co-injected isotope: nanophosphor systems are better suited for biological imaging applications. Furthermore, this strategy provides a more reliable means for evaluation of nanoparticle pharmacokinetics. Unmixed RL only images are shown in **Figure 5B** using a 620 nm emission filter. Application of the 620 nm emission filter resulted in a reduction of sig-

nal from spots (I) and (II) and disappearance of signal from spot (III), owing to the attenuation of the CL component in the emission signal. Thus, RL nanoprobes, internally excited by gamma rays from ^{89}Zr decay, display stronger luminescence over and above the CL signal of ^{89}Zr , thereby presenting a more clinically translatable system than those relying on CL alone.

Conclusion

In conclusion, we have reported a facile strategy for synthesis and surface modification of internally activatable, intrinsically radiolabeled, water soluble radioluminescent $[\text{}^{89}\text{Zr}]\text{Gd}_2\text{O}_2\text{S@PEG}$ nanophosphors. RLNPs promise several advantages over conventional optical agents, for biological imaging, such as greater tissue penetration, reduced autofluorescence and intrinsic multiplexing capabilities with radioimaging techniques. Incorporation of ^{89}Zr into the nanoparticle system improved the *in vivo* RL efficiency, by constantly keeping the scintillation source and the emitter in close proximity. Chelator-free ^{89}Zr labeling was found to be concentration, pH and temperature dependent. Systematic *in vitro* and *in vivo* studies demonstrated a strong binding affinity between ^{89}Zr and $\text{Gd}_2\text{O}_2\text{S@PEG}$ nanophosphors (corroborated by $< 2\%$ ID/g uptake in the bones over one week). This strategy can be generally applied to other metal oxides and oxysulfides, as well as other oxophilic isotopes, allowing for more robust *in vivo* pharmacokinetic profiling and biodistribution studies in the future. The presence of Gd^{3+} can be employed for T_1 -weighted MR imaging, underlining the excellent potential of these RLNPs as integrated multimodal PET/RL/MR imaging agents. With further improvements in nanoparticle modification and surface engineering, $[\text{}^{89}\text{Zr}]\text{Gd}_2\text{O}_2\text{S@PEG}$ can be tailored for tumor targeted imaging and therapy.

Acknowledgements

This work was supported, in part, by the University of Wisconsin-Madison, the National Institutes of Health (NIBIB/NCI R01CA169365, R01EB021336, P30CA014520), the American Cancer Society (125246-RSG-13-099-01-CCE), the National Natural Science Foundation of China (51102131), and the National Natural Science Foundation of Jiangxi Province, China (20142BAB216033).

Disclosure of conflict of interest

None.

Address correspondence to: Dr. Weibo Cai, Departments of Radiology and Medical Physics, School of Medicine and Public Health, University of Wisconsin-Madison, Room 7137, 1111 Highland Ave, Madison, WI 53705-2275, USA. Tel: 1-608-262-1749; Fax: 1-608-265-0614; E-mail: wcai@uwhealth.org

References

- [1] Sun C, Pratz G, Carpenter CM, Liu HG, Cheng Z, Gambhir SS and Xing L. Synthesis and radioluminescence of PEGylated Eu^{3+} -doped nanophosphors as bioimaging probes. *Adv Mater* 2011; 23: H195-H199.
- [2] Shen J, Sun LD and Yan CH. Luminescent rare earth nanomaterials for bioprobe applications. *Dalton Trans* 2008; 5687-5697.
- [3] Thirumalai J, Chandramohan R and Vijayan TA. Synthesis, characterization and formation mechanism of monodispersed $\text{Gd}_2\text{O}_2\text{S}:\text{Eu}^{3+}$ nanocrystals. *J Mater Sci: Mater Elec* 2011; 22: 936-943.
- [4] Chen H, Moore T, Qi B, Colvin DC, Jelen EK, Hitchcock DA, He J, Mefford OT, Gore JC, Alexis F and Anker JN. Monitoring pH-triggered drug release from radioluminescent nanocapsules with X-ray excited optical luminescence. *ACS Nano* 2013; 7: 1178-1187.
- [5] Song YH, You HP, Huang YJ, Yang M, Zheng YH, Zhang LH and Guo N. Highly uniform and monodisperse $\text{Gd}_2\text{O}_2\text{S}:\text{Ln}^{3+}$ ($\text{Ln} = \text{Eu}, \text{Tb}$) submicrospheres: solvothermal synthesis and luminescence properties. *Inorg Chem* 2010; 49: 11499-11504.
- [6] Osseni SA, Lechevallier S, Verelst M, Perriat P, Dexpert-Ghys J, Neumeyer D, Garcia R, Mayer F, Djanashvili K, Peters JA, Magdeleine E, Gros-Dagnac H, Celsis P and Mauricot R. Gadolinium oxysulfide nanoparticles as multimodal imaging agents for T_2 -weighted MR, X-ray tomography and photoluminescence. *Nanoscale* 2014; 6: 555-564.
- [7] Thorek DL, Ogirala A, Beattie BJ, Grimm J. Quantitative imaging of disease signatures through radioactive decay signal conversion. *Nat Med* 2013; 19: 1345-1350.
- [8] Carpenter CM, Sun C, Pratz G, Liu HG, Cheng Z and Xing L. Radioluminescent nanophosphors enable multiplexed small-animal imaging. *Opt Express* 2012; 20: 11598-11604.
- [9] Cao X, Chen XL, Kang F, Zhan YH, Cao X, Wang J, Liang JM and Tian J. Intensity enhanced cerenkov luminescence imaging using terbium-doped $\text{Gd}_2\text{O}_2\text{S}$ microparticles. *ACS Appl Mater Inter* 2015; 7: 11775-11782.

- [10] Hu ZH, Qu YW, Wang K, Zhang XJ, Zha JL, Song TM, Bao CP, Liu HX, Wang ZL, Wang J, Liu ZY, Liu HF and Tian J. In vivo nanoparticle-mediated radiopharmaceutical-excited fluorescence molecular imaging. *Nat Commun* 2015; 6: 1-12.
- [11] Ivanov RA, Korsakov IE, Formanovskii AA, Paramonov SE, Kuz'mina NP and Kaul AR. Heteroligand lanthanide dialkyldithiocarbamate complexes with 1,10-phenanthroline: a new approach to synthesis and application for the preparation of sulfides. *Russ J Coord Chem* 2002; 28: 670-672.
- [12] Zhao F and Gao S. Pyrolysis of single molecular precursor for monodisperse lanthanide sulfide/oxysulfide nanocrystals. *J Mater Chem* 2008; 18: 949-953.
- [13] Zhao F, Yuan M, Zhang W and Gao S. Monodisperse lanthanide oxysulfide nanocrystals. *J Am Chem Soc* 2006; 128: 11758-11759.
- [14] Zhang Y, Hong H, Severin GW, Engle JW, Yang YA, Goel S, Nathanson AJ, Liu G, Nickles RJ, Leigh BR, Barnhart TE and Cai W. ImmunoPET and near-infrared fluorescence imaging of CD105 expression using a monoclonal antibody dual-labeled with Zr-89 and IRDye 800CW. *Amer J Transl Res* 2012; 4: 333-346.
- [15] Thirumalai J, Chandramohan R, Divakar R, Mohandas E, Sekar M and Parameswaran P. Eu 3+ doped gadolinium oxysulfide (Gd_2O_3) nanostructures-synthesis and optical and electronic properties. *Nanotechnology* 2008; 19: 1-7.
- [16] Li LL, Zhang R, Yin L, Zheng K, Qin W, Selvin PR and Lu Y. Biomimetic surface engineering of lanthanide-doped upconversion nanoparticles as versatile bioprobes. *Angew Chem Int Ed Engl* 2012; 51: 6121-6125.
- [17] Liu H, Zhang X, Xing B, Han P, Gambhir SS and Cheng Z. Radiation-luminescence-excited quantum dots for in vivo multiplexed optical imaging. *Small* 2010; 6: 1087-1091.
- [18] Chen F, Goel S, Valdovinos HF, Luo HM, Hernandez R, Barnhart TE and Cai W. In vivo integrity and biological fate of chelator-free zirconium-89-labeled mesoporous silica nanoparticles. *ACS Nano* 2015; 9: 7950-7959.
- [19] Goel S, Chen F, Luan S, Valdovinos HF, Shi S, Graves SA, Ai F, Barnhart TE, Theuer CP and Cai W. Engineering intrinsically zirconium-89 Radiolabeled self-destructing mesoporous silica nanostructures for in vivo biodistribution and tumor targeting studies. *Adv Sci (Weinh)* 2016; 3: 1600122.
- [20] Abou DS, Ku T and Smith-Jones PM. In vivo biodistribution and accumulation of ^{89}Zr in mice. *Nucl Med Biol* 2011; 38: 675-681.
- [21] Chen F, Goel S, Hernandez R, Graves SA, Shi S, Nickles RJ and Cai W. Dynamic positron emission tomography imaging of renal clearable gold nanoparticles. *Small* 2016; 12: 2775-2782.

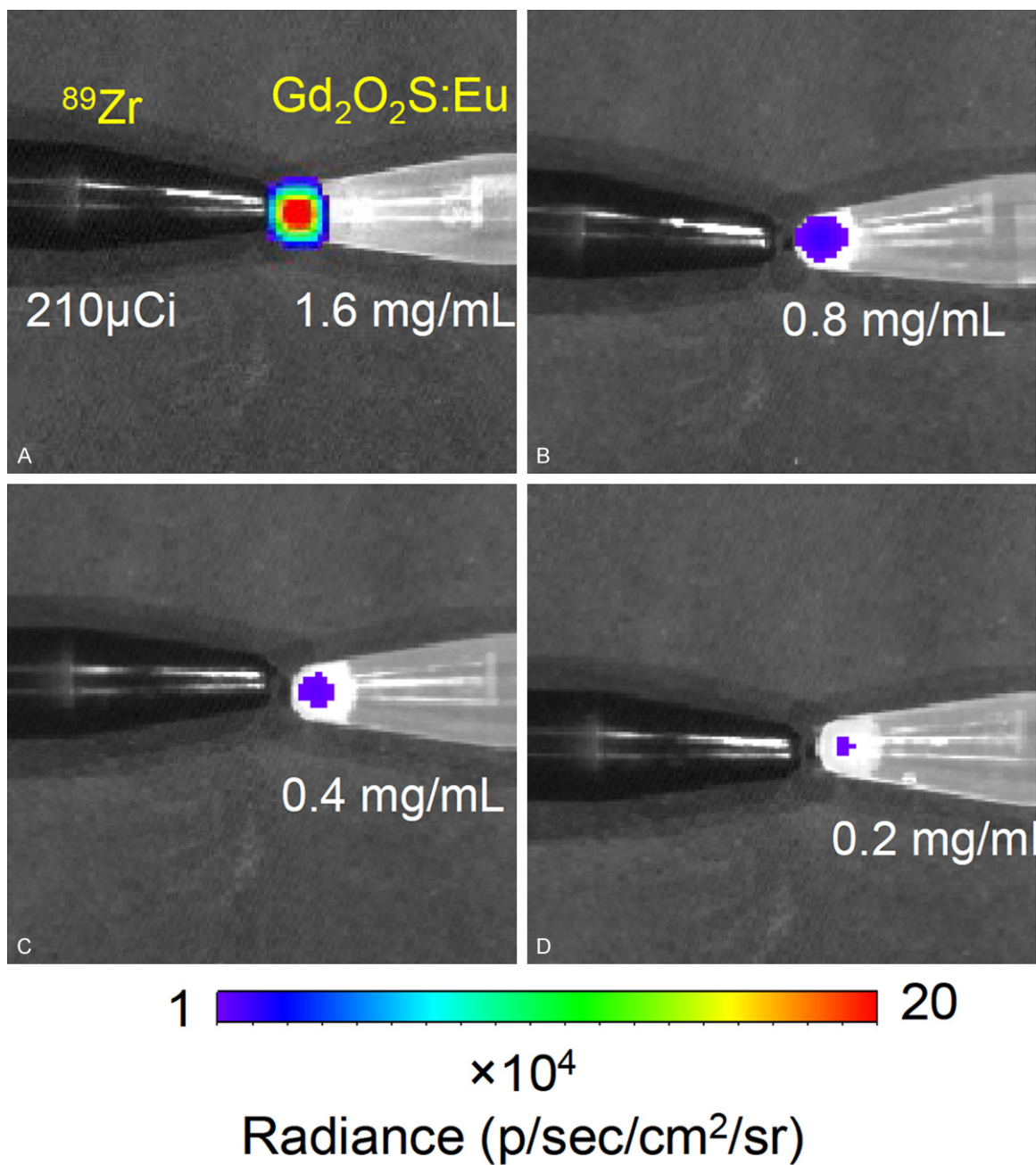


Figure S1. Variation of ^{89}Zr -activated radioluminescence signal as a function of $\text{Gd}_2\text{O}_2\text{S}:\text{Eu}$ nanophosphor concentration; (A) 1.6 mg/mL, (B) 0.8 mg/mL, (C) 0.4 mg/mL, and (D) 0.2 mg/mL. (Ex: Closed, Em: 620 nm).

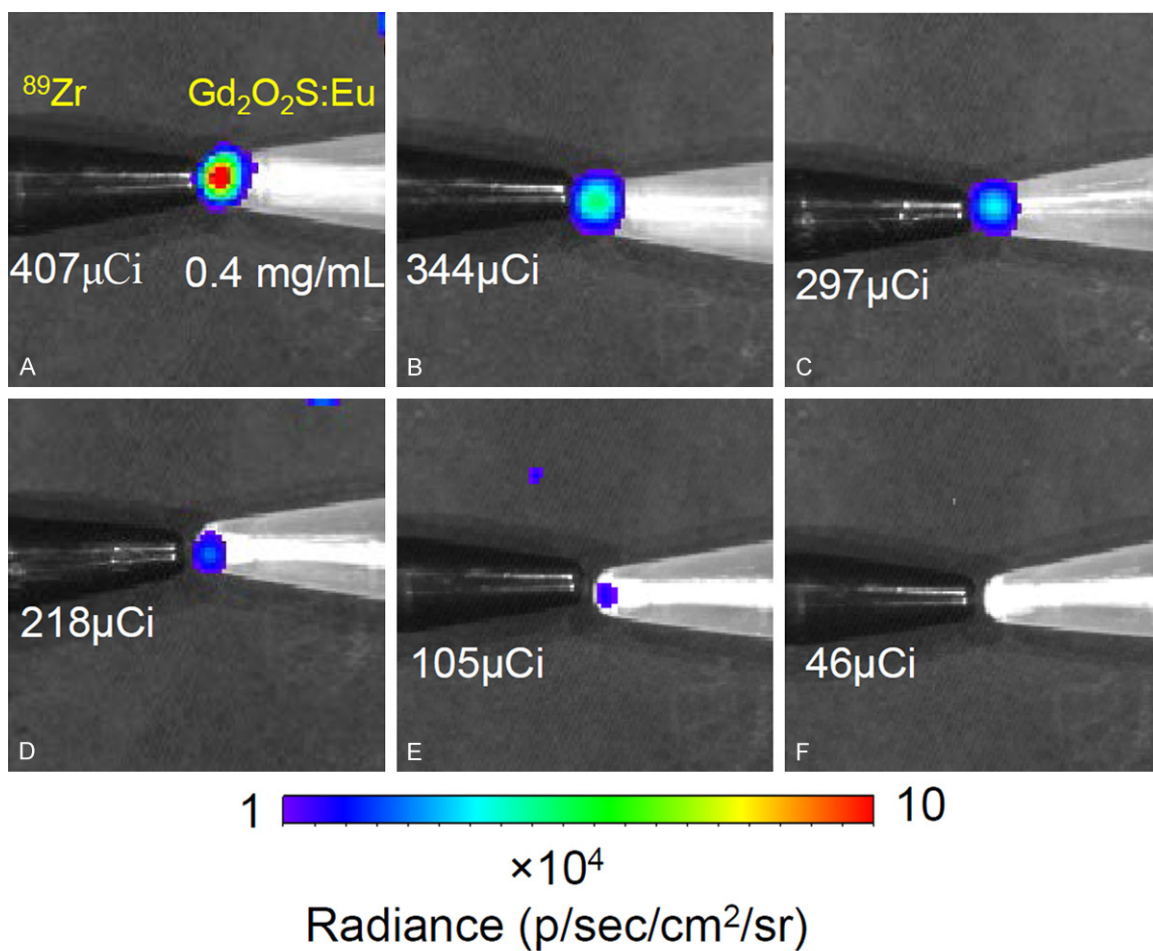


Figure S2. Variation of ^{89}Zr -activated radioluminescence signal from $\text{Gd}_2\text{O}_2\text{S}:\text{Eu}$ nanophosphors, as a function of radioactive dose of ^{89}Zr . (A) 407 μCi , (B) 344 μCi , (C) 297 μCi , (D) 218 μCi , (E) 105 μCi , and (F) 46 μCi ^{89}Zr . (Ex: Closed, Em: 620 nm).

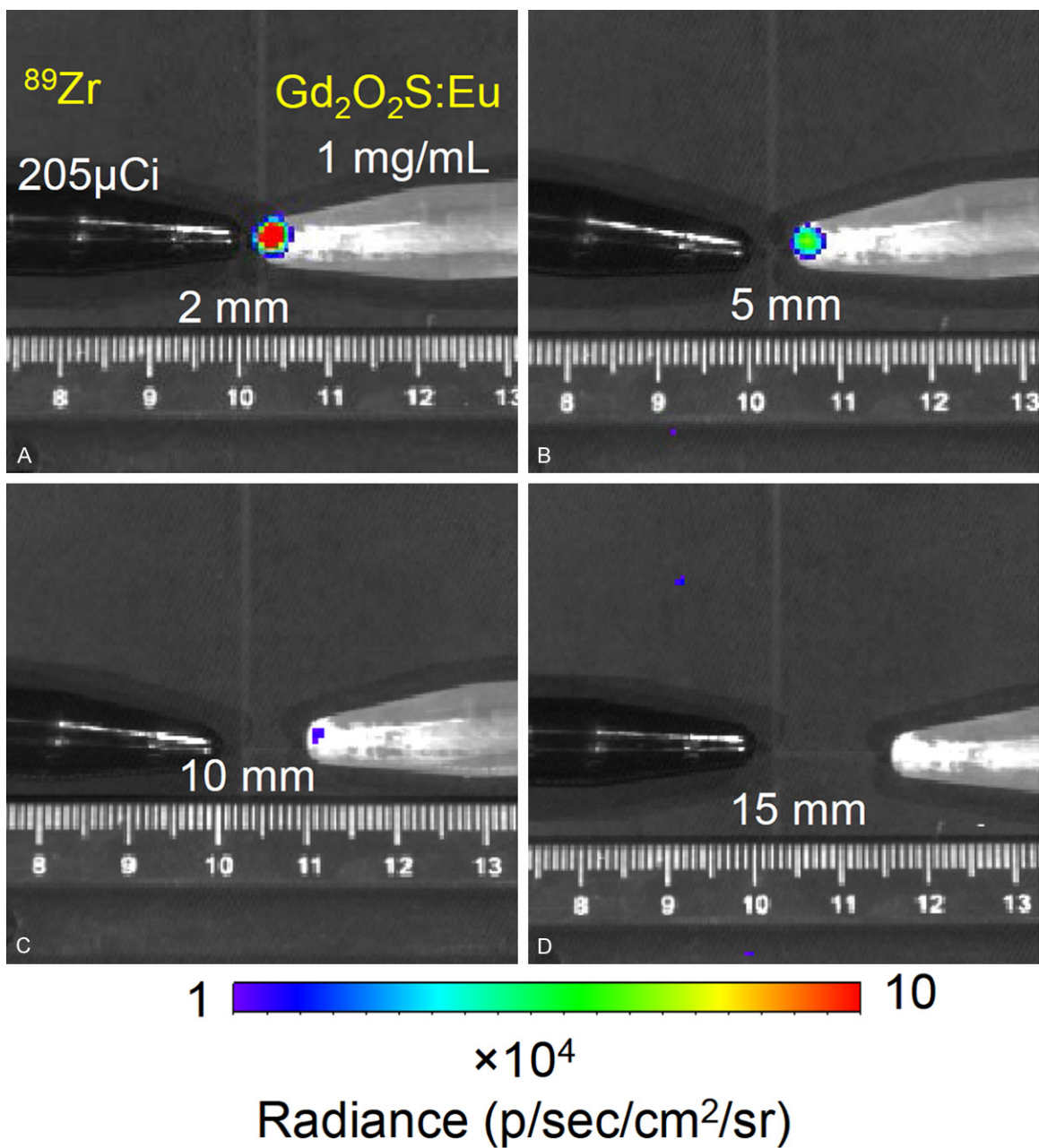


Figure S3. Variation of ^{89}Zr -activated radioluminescence signal from $\text{Gd}_2\text{O}_2\text{S:Eu}$ nanophosphors with increasing distance between the excitation source (^{89}Zr) and emitter ($\text{Gd}_2\text{O}_2\text{S:Eu}$); (A) 2 mm, (B) 5 mm, (C) 10 mm, and (D) 15 mm. (Ex: Closed, Em: 620 nm).

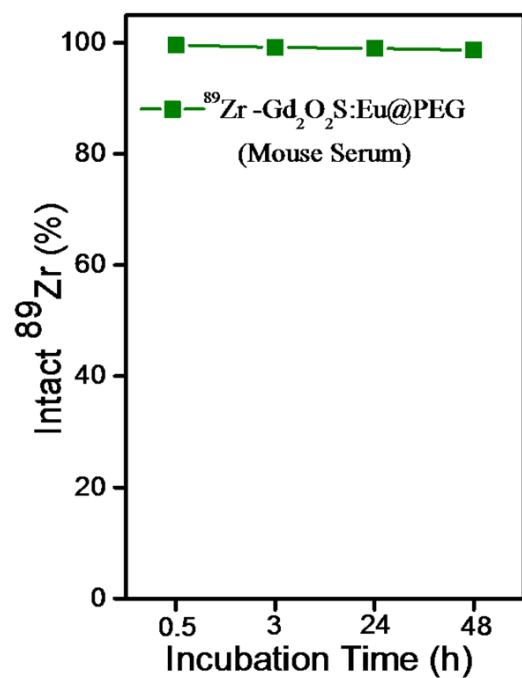


Figure S4. In vitro radiostability test of [^{89}Zr]Gd₂O₂S:Eu in whole mouse serum at 37 °C over 48 h.